INTERNATIONAL JOURNAL FOR NUMERICAL METHODS IN FLUIDS, VOL. 23, 567–588 (1996)

A MULTIBLOCK IMPLEMENTATION OF A NON-ORTHOGONAL, COLLOCATED FINITE VOLUME ALGORITHM FOR COMPLEX TURBULENT FLOWS

F. S. LIEN, W. L. CHEN AND M. A. LESCHZINER

University of Manchester Institute of Science and Technology (UMIST), PO Box 88, Manchester M60 1QD, U.K.

SUMMARY

A multiblock algorithm for general 2D and 3D turbulent flows is introduced and applied to three cases: a compressor cascade passage, a two-element high-lift aerofoil and a round-to-square transition duct. The method is a generalization of a single-block scheme which is based on a non-orthogonal, fully collocated finite volume framework, applicable to incompressible and compressible flows and incorporating a range of turbulence transport models, including second-moment closure. The multiblock implementation is essentially block-unstructured, each block having its own local co-ordinate system unrelated to those of its neighbours. Any one block may interface with more than one neighbour along any one block face. Interblock communication is handled by connectivity matrices and effected via a two-cell overlap region along block boundaries in which halo data reside. The algorithm and the associated data communication are explained in detail, and its effectiveness is verified, with particular reference to improved numerical resolution and parallel computing.

KEY WORDS: multiblock; turbulent flow; computational modelling; parallel computing

1. INTRODUCTION

Geometric flexibility is one of the key ingredients in the mix of capabilities allowing computational fluid dynamics (CFD) to be used as a practical aid to engineering design. It is also of increasing importance in the context of validation efforts focusing on geometrically and physically complex turbulent flows, especially in high-lift aerodynamics and highly loaded turbomachine blades in which turbulence transport contributes significantly to the primary operational characteristics.

Although a considerable level of flexibility can be attained with single-block structured grids (provided non-orthogonality is admitted), there are many applications, notably such involving multiply connected domains, which cannot be meshed with a single structured grid. Alternative routes to increasing geometric flexibility are based on unstructured and block-structured grids. Both have strengths and weaknesses. With the latter option, local flow-driven adaptation is difficult. However, this option is well-disposed towards an accurate near-wall resolution, allows the use of well-established structured-grid solvers (e.g. ADI, ICCG, SIP, multigrid), is well-suited to parallel computing based on domain-decomposition methods, and permits the use of a simple index connectivity which enhances transparency and eases programming. Adaptation can be implemented by use of local mesh refinement and embedding strategies (e.g. References 1–3), although this

CCC 0271–2091/96/060567–22

Received August 1995
Revised January 1996

usually necessitates the introduction of 'hanging nodes' and the application of elaborate interpolation practices which ensure satisfaction of the conservation principle across mesh-interface planes.

The objective of this paper is to describe in detail a multiblock implementation of a general non-orthogonal finite volume algorithm for 2D and 3D turbulent flows (STREAM[4]). The block topology is essentially unstructured, with a block-connectivity matrix generated to allow efficient interblock communication. Within each block, the grid is fully structured, however. One notable feature of the method is that the co-ordinate systems, governing equations and physical models need not be (indeed, are not) identical across the entire block family, a characteristic which is particularly beneficial in external aerodynamics applications in which large, nearly inviscid regions coexist with thin boundary layers and complex separated zones.

The remainder of the paper is divided into two principal sections. First, the numerical details of extending a single-block algorithm to a multiblock strategy are addressed. This includes the construction of the connectivity matrix, the exchange of 'halo data' and the design of the data structure. This is followed by several verification and validation tests for 2D as well as 3D cases, wherein multiblock solutions are contrasted with experimental data and, where appropriate, with single-block ones to demonstrate the validity of the multiblock implementation.

2. DESCRIPTION OF A MULTIBLOCK ALGORITHM

2.1. Basic numerical framework

The multiblock strategy takes as its starting point a single-block scheme which solves the Reynolds-averaged Navier–Stokes equations, the mass conservation law and the appropriate turbulence-model equations. The finite volume discretization procedure and the implementation of turbulence models up to full second-moment closure, within the single-block algorithm, for both incompressible and compressible (transonic) flows, have been presented in detail by Lien and Leschziner.[4] Here, only those facets are summarized that impinge on the multiblock extension to follow in Section 2.2. To simplify the statement without, however, introducing a significant loss of generality, attention is focused on two-dimensional steady flow. The extension to a three-dimensional framework is fairly straightforward.

Integration of any transport equation governing a flow property ϕ over the volume shown in Figure 1 and application of the Gauss divergence theorem result in a balance of convective and diffusive cell

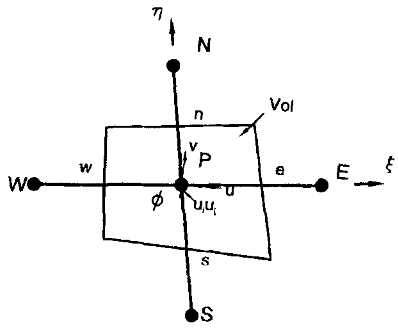

Figure 1. Non-orthogonal 2D finite volume with collocated storage arrangement

face fluxes and volume-integrated net source. The introduction of approximations which link the convective and diffusive fluxes to nodal values leads to a weighted-average formula of the form

$$A_{\mathrm{P}}\phi_{\mathrm{P}} = \sum_{m=\mathrm{E,W,N,S}} A_m \phi_m + S_\phi, \tag{1}$$

where ϕ stands either for momentum components or for any intensive scalar property, including transported turbulence quantities, and S_ϕ represents the source/sink term. In the present implementation, either the QUICK scheme of Leonard[5] or the UMIST-TVD scheme of Lien and Leschziner[6] has been used for convection, while the diffusive fluxes have been approximated by central differences. Whatever approximations are adopted for transport, equation (1) applies, provided that the source term is made to accommodate all links to nodes lying beyond the compact five-point stencil P, E, W, N, S. In the present scheme, any higher-order convection scheme is implemented as a first-order upwind approximation augmented by deferred corrections which are lumped in the source term S_ϕ. The coefficients A_m thus become

$$\begin{aligned}
A_{\mathrm{E}} &= [\Gamma_\phi J(\xi_x\xi_x + \xi_y\xi_y)]_{\mathrm{e}} + \mathrm{MAX}(-\rho U, 0)_{\mathrm{e}},\\
A_{\mathrm{W}} &= [\Gamma_\phi J(\xi_x\xi_x + \xi_y\xi_y)]_{\mathrm{w}} + \mathrm{MAX}(\rho U, 0)_{\mathrm{w}},\\
A_{\mathrm{N}} &= [\Gamma_\phi J(\eta_x\eta_x + \eta_y\eta_y)]_{\mathrm{n}} + \mathrm{MAX}(-\rho V, 0)_{\mathrm{n}},\\
A_{\mathrm{S}} &= [\Gamma_\phi J(\eta_x\eta_x + \eta_y\eta_y)]_{\mathrm{s}} + \mathrm{MAX}(\rho V, 0)_{\mathrm{s}},\\
A_{\mathrm{P}} &= A_{\mathrm{E}} + A_{\mathrm{W}} + A_{\mathrm{N}} + A_{\mathrm{S}} - S_{\mathrm{P}},
\end{aligned} \tag{2}$$

where the contravariant velocities are given by

$$U = J(u\xi_x + v\xi_y), \qquad V = J(u\eta_x + v\eta_y) \tag{3}$$

and $S_{\mathrm{P}}\phi_{\mathrm{P}}$ combines all negative fragments of S_ϕ. The component relationship between the natural and dual base vectors is

$$\xi_x = y_\eta / J, \qquad \xi_y = -x_\eta / J, \qquad \eta_x = -y_\xi / J, \qquad \eta_y = x_\xi / J, \tag{4}$$

with $J = x_\xi y_\eta - x_\eta y_\xi$. With the UMIST-TVD scheme used for convection, the deferred corrector 'source' S_ϕ^{DC} in (1) is

$$\begin{aligned}
S_\phi^{\mathrm{DC}} = 0{\cdot}5\{&[(\rho U)_{\mathrm{e}}^+ \varphi(r_{\mathrm{e}}^+) - (\rho U)_{\mathrm{e}}^- \varphi(r_{\mathrm{e}}^-)](\phi_{\mathrm{E}} - \phi_{\mathrm{P}})\\
&- [(\rho U)_{\mathrm{w}}^+ \varphi(r_{\mathrm{w}}^+) - (\rho U)_{\mathrm{w}}^- \varphi(r_{\mathrm{w}}^-)](\phi_{\mathrm{P}} - \phi_{\mathrm{W}})\\
&+ [(\rho V)_{\mathrm{n}}^+ \varphi(r_{\mathrm{n}}^+) - (\rho V)_{\mathrm{n}}^- \varphi(r_{\mathrm{n}}^-)](\phi_{\mathrm{N}} - \phi_{\mathrm{P}})\\
&- [(\rho V)_{\mathrm{s}}^+ \varphi(r_{\mathrm{s}}^+) - (\rho V)_{\mathrm{s}}^- \varphi(r_{\mathrm{s}}^-)](\phi_{\mathrm{P}} - \phi_{\mathrm{S}})\},
\end{aligned} \tag{5}$$

in which $\varphi(r)$ is defined as

$$\varphi(r) = \max[0, \min(2r, 0{\cdot}25 + 0{\cdot}75r, \underbrace{0{\cdot}75 + 0{\cdot}25r}_{\text{QUICK}}, 2)], \tag{6}$$

$$(\rho U)^\pm = (\rho U \pm |\rho U|)/2, \qquad (\rho V)^\pm = (\rho V \pm |\rho V|)/2 \tag{7}$$

and $r_{\mathrm{e,w,n,s}}^\pm$ are (see Figure 2)

$$\begin{aligned}
r_{\mathrm{e}}^+ &= \frac{\phi_{\mathrm{P}} - \phi_{\mathrm{W}}}{\phi_{\mathrm{E}} - \phi_{\mathrm{P}}}, &
r_{\mathrm{e}}^- &= \frac{\phi_{\mathrm{E}} - \phi_{\mathrm{EE}}}{\phi_{\mathrm{P}} - \phi_{\mathrm{E}}}, &
r_{\mathrm{w}}^+ &= \frac{\phi_{\mathrm{W}} - \phi_{\mathrm{WW}}}{\phi_{\mathrm{P}} - \phi_{\mathrm{W}}}, &
r_{\mathrm{w}}^- &= \frac{\phi_{\mathrm{P}} - \phi_{\mathrm{E}}}{\phi_{\mathrm{W}} - \phi_{\mathrm{P}}},\\
r_{\mathrm{n}}^+ &= \frac{\phi_{\mathrm{P}} - \phi_{\mathrm{S}}}{\phi_{\mathrm{N}} - \phi_{\mathrm{P}}}, &
r_{\mathrm{n}}^- &= \frac{\phi_{\mathrm{N}} - \phi_{\mathrm{NN}}}{\phi_{\mathrm{P}} - \phi_{\mathrm{N}}}, &
r_{\mathrm{s}}^+ &= \frac{\phi_{\mathrm{S}} - \phi_{\mathrm{SS}}}{\phi_{\mathrm{P}} - \phi_{\mathrm{S}}}, &
r_{\mathrm{s}}^- &= \frac{\phi_{\mathrm{P}} - \phi_{\mathrm{N}}}{\phi_{\mathrm{S}} - \phi_{\mathrm{P}}}.
\end{aligned} \tag{8}$$

To impose mass conservation in both incompressible and compressible conditions, the SIMPLE pressure-correction algorithm of Patankar[7] is adopted. Checkerboard oscillations arising from the collocated storage arrangement can be avoided by use of Rhie and Chow's interpolation.[8] Although this scheme is well-known, its principal elements need to be highlighted here, at least in simple terms, to aid understanding of a particular facet of the multiblock extension to follow. The essential arguments may be conveyed by reference to a simple one-dimensional form of the discretized equation pertaining to the cell in Figure 3. The key point is that the face velocity u_e is evaluated by linear interpolation of the momentum equations governing the nodal velocities u_P and u_E from which then the pressure-gradient terms are subtracted and to which a compensating pressure-gradient fragment is finally added, the last formed only with the two nodal pressures straddling the face velocity u_e. The result is then

$$\begin{aligned} u_e = {} & \underbrace{\tfrac{1}{2}(u_P + u_E)}_{\text{linear interpolation}} \\ & + \underbrace{\tfrac{1}{2}\{[(DU/A_P)_P + (DU/A_P)_E](p_P - p_E) - [(DU/A_P)(p_w - p_e)]_P - [(DU/A_P)(p_w - p_e)]_E\}}_{\text{pressure smoothing}}, \end{aligned} \tag{9}$$

where DU_m is the u-directed cross-sectional area at location m ($m = \text{P, E}$). An important point to underline in relation to (9) is that the face velocity u_e depends upon pressure values at four nodes, two on either side of the face. This has implications as regards interblock connectivity and data transfer. As an aside, it is instructive to note that with the assumption $DU_P = DU_E$ and $(A_P)_P = (A_P)_E$ and a linear interpolation of p_e and p_w, the 'pressure-smoothing' term in (9) turns out to be

$$(DU/4A_P)(p_{EE} - 3p_E + 3p_P - p_W), \tag{10}$$

which is, in essence, a third-order artificial dissipation term. Since the face velocity u_e enters the convective flux $u_e(\rho u)\Delta y$ of the u-momentum equation, interpolation of (9) introduces a fourth-order smoothing term into the momentum equation, even if $\partial p/\partial x$ is approximated by central differencing. The pressure-correction equation arises upon decomposing the correct face velocity u_e into an estimated value, obtained with an approximate pressure field, and a corrective perturbation:

$$u_e = u_e^* + u_e', \tag{11}$$

where the superscript * denotes the approximate value and $u_e' \sim (DU/AP)_e(p_P' - p_E')$, with the subscript 'e' in the RHS multiplier denoting a centred average of the values at the two neighbouring nodes on either side of the face. Substitution of (11) and analogous expressions for other face-

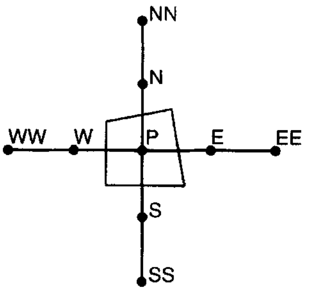

Figure 2. Nine-point stencil for QUICK and UMIST-TVD schemes

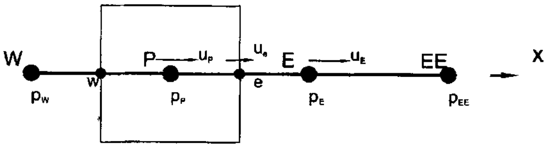

Figure 3. Finite volume cell in one-dimensional mesh

velocity components into the continuity equation for the cell in Figure 1, yields the pressure-correction equation

$$a_P p'_P = \sum_{m=E,W,N,S} a_m p'_m + R_m, \tag{12}$$

where

$$\begin{aligned} a_E &= \rho_e(x_\eta^2 + y_\eta^2)_e/(A_P)_e, \\ a_W &= \rho_w(x_\eta^2 + y_\eta^2)_w/(A_P)_w, \\ a_N &= \rho_n(x_\xi^2 + y_\xi^2)_n/(A_P)_n, \\ a_S &= \rho_s(x_\xi^2 + y_\xi^2)_s/(A_P)_s, \\ a_P &= \sum_{m=E,W,N,S} a_m, \end{aligned} \tag{13}$$

with the mass imbalance R_m defined by

$$R_m = U_w^* - U_e^* + V_s^* - V_n^*. \tag{14}$$

2.2. *Multiblock implementation*

The multiblock algorithm is based essentially on a subdivision of the solution domain into an arbitrary number of contiguous, non-overlapping blocks, each having its own grid and associated local co-ordinate system. Each grid is first generated separately by use of any suitable grid-generation procedure, the only constraint being continuity in grid-line positions across the block boundaries. Each block, looked at in isolation, is then surrounded by an 'auxiliary' layer of two cells originating from neighbouring blocks. In effect, the block is made to penetrate into its neighbours to the extent of two cell intervals in order to accommodate 'halo data' which are needed for the solution within the block in question. The choice of a two-cell penetration is linked to the nature of the higher-order convection scheme and the Rhie and Chow interpolation practice (equations (5)–(8) and (9)). Although the co-ordinate systems of neighbouring blocks can be quite different in orientation, as is exemplified in Figure 4 by blocks 2 and 3, all geometric data pertaining to the auxiliary layer attached to the parent block, including the metric tensors and the Jacobian, are treated in terms of the co-

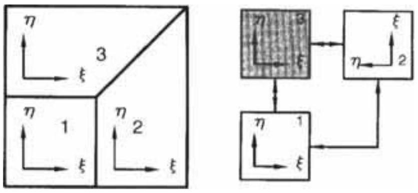

Figure 4. Multiblock arrangement with different local co-ordinate systems

ordinate system of the parent block and stored as if the layer were part of the block. This arrangement obviates, with one exception noted below, the need for any one block to directly access the 'foreign' geometric information and mass fluxes residing in neighbouring blocks during the solution process within the block.

Interblock connectivity is handled by a connectivity matrix in the form of the 2D array MATRIX(BLOCK, FACE), where BLOCK is the block number being considered, FACE identifies the block face (ranging from 1 to 4, with 1 denoting the eastern face, 2 the western face, etc.) and MATRIX identifies the block sharing FACE with BLOCK. The co-ordinate system relating to any one block is stored in the form of COORD(BLOCK, FACE), representing all possible co-ordinate permutations in the neighbouring block sharing the face 'FACE'. A typical example for COORD is given in Figure 5. The neighbouring right-hand side block can have any one of eight combinations of coordinates, and this is signified by the integers 1–8. Another more general example illustrating the use of both MATRIX and COORD is given below by reference to Figure 4, where

$$\begin{aligned} &\text{MATRIX}(3,1)=2, \qquad &&\text{MATRIX}(3,2)=0,\\ &\text{MATRIX}(3,3)=0, \qquad &&\text{MATRIX}(3,4)=1 \end{aligned}$$

and

$$\begin{aligned} &\text{COORD}(3,1)=8, \qquad &&\text{COORD}(3,2)=0,\\ &\text{COORD}(3,3)=0, \qquad &&\text{COORD}(3,4)=1. \end{aligned}$$

In the above, the value '0' signifies that the neighbouring block is a physical (real) boundary of the solution domain.

Reference to (9), (12) and (13) shows that the coefficients in the pressure-correction equation depend on the A_P-value associated with the momentum equations applied to the cell over which mass conservation is to be satisfied as well as to neighbouring cells on either side in any co-ordinate direction. It is crucial, therefore, to transmit this quantity from the neighbouring blocks into the auxiliary two-cell layer when solving the momentum equations in the parent block. This transfer is greatly assisted by the fact that A_P is co-ordinate-invariant, i.e. independent of the block-local co-ordinate system. To demonstrate this, attention is focused on the cell shown in Figure 6, associated with two different local co-ordinate systems. The mass fluxes on the eastern and northern faces may be evaluated by combining (3) and (4), in conjunction with the assumption that $\Delta\xi=\Delta\eta=1$, as follows: for co-ordinate system (a),

$$\begin{aligned} U_e &= -u_{12}\Delta y_{12} + v_{12}\Delta x_{12}, \qquad & U_w &= u_{34}\Delta y_{34} - v_{34}\Delta x_{34},\\ V_n &= -u_{23}\Delta y_{23} + v_{23}\Delta x_{23}, \qquad & V_s &= u_{41}\Delta y_{41} - v_{41}\Delta x_{41}; \end{aligned} \tag{15}$$

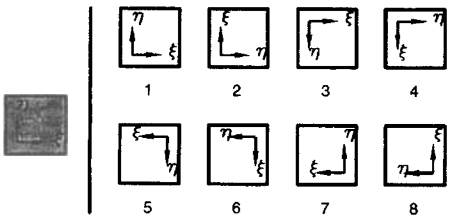

Figure 5. All possible permutations of local co-ordinate systems in blocks adjacent to any reference block

for co-ordinate system (b),

$$\begin{aligned} U_\mathrm{e} &= -u_{23}\Delta y_{23} + v_{23}\Delta x_{23}, & U_\mathrm{w} &= u_{41}\Delta y_{41} - v_{41}\Delta x_{41}, \\ V_\mathrm{n} &= -u_{34}\Delta y_{34} + v_{34}\Delta x_{34}, & V_\mathrm{s} &= u_{12}\Delta y_{12} - v_{12}\Delta x_{12}. \end{aligned} \tag{16}$$

Here, $\Delta x_{mn} = x_m - x_n$ and $\Delta y_{mn} = y_m - y_n$ $(1 \leqslant m, n \leqslant 4)$. The diffusion coefficients, on the other hand, can be written as:

for co-ordinate system (a),

$$\begin{aligned} D_\mathrm{e} &= (\Gamma_\phi/J)_\mathrm{e}\Delta_{12}^2, & D_\mathrm{w} &= (\Gamma_\phi/J)_\mathrm{w}\Delta_{34}^2, \\ D_\mathrm{n} &= (\Gamma_\phi/J)_\mathrm{n}\Delta_{23}^2, & D_\mathrm{s} &= (\Gamma_\phi/J)_\mathrm{s}\Delta_{41}^2; \end{aligned} \tag{17}$$

for co-ordinate system (b),

$$\begin{aligned} D_\mathrm{e} &= (\Gamma_\phi/J)_\mathrm{e}\Delta_{23}^2, & D_\mathrm{w} &= (\Gamma_\phi/J)_\mathrm{w}\Delta_{41}^2, \\ D_\mathrm{n} &= (\Gamma_\phi/J)_\mathrm{n}\Delta_{34}^2, & D_\mathrm{s} &= (\Gamma_\phi/J)_\mathrm{s}\Delta_{12}^2. \end{aligned} \tag{18}$$

Here, $\Delta_{mn}^2 = \Delta x_{mn}^2 + \Delta y_{mn}^2$. Since ($J_\mathrm{e}$, J_w, J_n, J_s) in co-ordinate system (a) are the same as (J_s, J_n, J_e, J_w) in co-ordinate system (b) and $S_\mathrm{P} = 0$ in the momentum equations, the end results for A_P obtained by substituting either (15) and (17) or (16) and (18) into (2) are identical.

Once the coefficients for the transport and pressure-correction equations have been assembled for each block, the resulting systems of equations are solved in a segregated manner in the following sequence:

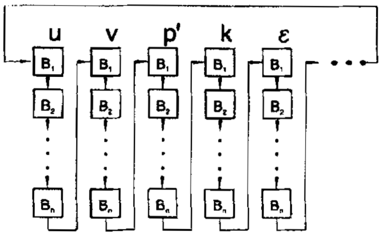

Each set of equations pertaining to any one block is solved within an 'inner iteration' by Stone's SIP or the ADI method concurrently with the temporarily 'frozen' block-boundary conditions in the 'halo' region. Then, an update of boundary conditions is effected, via the connectivity matrix and the identifiers of the co-ordinate systems in neighbouring blocks, in order to establish the interblock coupling. An 'outer iteration' consists of the solution of any one set of equations over all blocks and associated exchange of data across block boundaries. This sweep is arranged as a block-Jacobi method. This sequence is then repeated for all flow properties and may be expressed by the following FORTRAN code fragment:

```
DO NS = 1,NO-of-SWEEPS⇐outer iteration
DO NB = 1,NO-of-BLOCKS
CALL MATRIX-SOLVER(NB, φ)⇐inner iteration
END DO
DO NB = 1,No-of-BLOCKS
CALL MESSAGE-PASS(NB, φ)
END DO
END DO
```

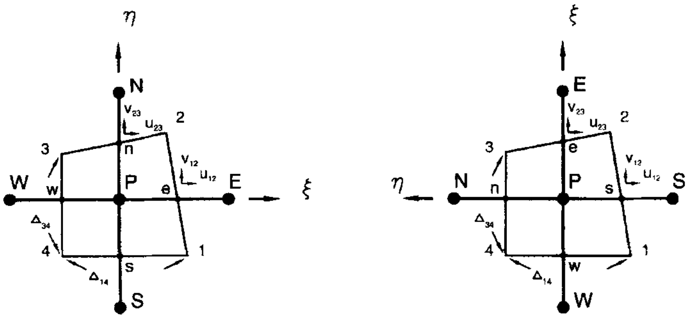

(a) (b)

Figure 6. Identical finite volumes but with different local co-ordinate systems

One advantage of using the above structure when running the algorithm on a (virtual) shared-memory computer, such as the multiprocessor Cray YMP, is that DO-loop NB can be parallelized, e.g. by inserting a CFPP$ CNCALL compiler directive above this loop. The inner loop contained in the matrix solver, such as a tridiagonal matrix algorithm combined with a 'red and black' colouring technique, can easily be vectorized. Since the 'halo data' are exchanged via the connectivity matrix, it is advantageous to insert a CFPP$ NODEPCHK compiler directive which enforces vectorization in the MESSAGE-PASS subroutine. To demonstrate the significance of the above step, the solution of a Laplace equation is considered. The computational domain, containing 32 × 32 × 32 grid lines, is decomposed into 4 × 4 × 4 (= 64) blocks. The program is compiled with an option which activates the 'autotasking' mode of the Cray YMP (see Cray Manual SG-3074 5.0 for details). The speed-up values attained on eight processors, with and without inserting the parallelizing and vectorizing compiler directives, are shown in Figure 7, and the compilation listing associated with the former is

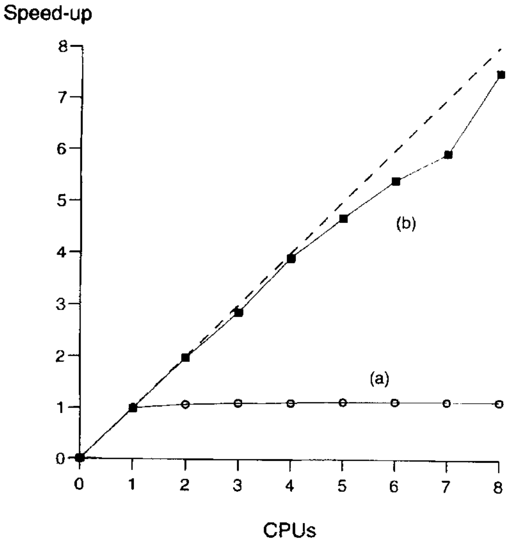

Figure 7. Speed-up characteristics with multitasking on Cray YMP[8] (a) without and (b) with parallel compiler directives

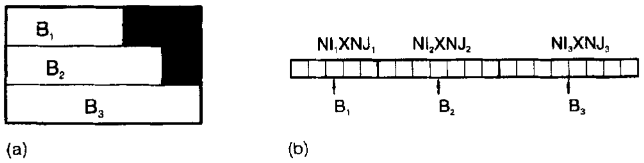

Figure 8. Two options for block data storage in memory

given in the Appendix. As can be seen, use of the directives results in a dramatic increase in speed-up from 1·13/8 to 7·54/8.

Two kinds of data structure for storing the variables have been studied, and both are shown schematically in Figure 8. The first one, represented by Figure 8(a), has been adopted by Lien and Leschziner[9] in their implementation of a multigrid method. The advantage of this data structure is that the *I–J* index structure can be retained, which considerably reduces the effort in programming the discretized equations. However, a major drawback is that the memory portions to be allocated to associated blocks need to be prearranged manually in order to maximize the utilization of memory space—an approach which can be very laborious when the number of blocks is large or the size of the blocks varies greatly across the solution domain. The alternative arrangement in which data in blocks are stored contiguously in a one-dimensional array, as illustrated in Figure 8(b), avoids the above drawback. In the present study, both methods were investigated. For the case of the NLR 7301 multi-element aerofoil to be considered in Section 3.3, the saving of memory allocation achieved by use of the data structure in Figure 8(b) relative to that in Figure 8(a) is 17 per cent.

3. APPLICATION

3.1. Introductory remarks

This section is concerned with the validation of the multiblock scheme and its application, in conjunction with advanced turbulence models, to two- and three-dimensional flows of industrial relevance. The first example is a highly loaded 2D 'controlled diffusion' (CD) compressor-cascade blade operating at a Reynolds number of 7×10^5, based on the inflow velocity and chord length. Global as well as local experimental data have been obtained for this case by Elazar and Shreeve.[10] This case is used first to validate the correctness of the data-exchange algorithm by use of the 'halo' region in the context of a domain-decomposition implementation. Then, results obtained with a single-block and a multiblock H-grid as well as a hybrid H/O-multiblock grid, the latter featuring a change in co-ordinate orientation across block boundaries, are compared with each other. Finally, the multiblock strategy is used to investigate the performance of turbulence closures, including a non-linear eddy-viscosity model, by reference to experimental data.

The second two-dimensional case investigated is the NLR 7301 two-element aerofoil for which measurements have been performed by van den Berg[11] and Gooden and van Lent.[12] The distinctive feature of this case, as far as block-connectivity is concerned, is that one block can interface with more than two others along any one block face, requiring the modification of the MATRIX and COORD arrays mentioned in Section 2. The flap deflection angle δ_F is 20°, and the Reynolds number, based on the freestream velocity and the chord of the wing, is $2{\cdot}5 \times 10^6$. The particular condition chosen for the present calculation is one in which the minimum distance between the wing trailing edge and the flap upper surface—the 'gap'—equals to 2·6 per cent of the chord at the main aerofoil incidence $\alpha = 13{\cdot}1°$.

The last case examines an extension of the above multiblock scheme to three-dimensional conditions. The geometry considered is a circular-to-rectangular (CR) transition duct, examined experimentally by Davis and Gessner.[13] The Reynolds number, based on the inlet bulk velocity and inlet diameter, is $3\cdot 9 \times 10^5$. The computational domain extends from $1D$ upstream of the transition entry to $3\cdot 5D$ downstream of its exit. At the inlet, velocity and turbulence-energy profiles were prescribed on the basis of experimental data. The dissipation rate has been extracted from the mixing length argument. At the exit, a fully developed flow condition is assumed.

3.2. CD compressor cascade

To verify that interblock communication operates correctly, this flow has been computed with the H-type mesh shown in Figure 9, treated in one computation as a single block and in the other as a multiblock arrangement. For correctness of implementation to be verified, both solutions must be shown to be identical. Thus, Figure 10 compares pressure contours and demonstrates that both meshes result in the same solution.

Computational solutions are generally claimed to be free from numerical error if they are insensitive to grid density and disposition. This condition is often extremely difficult to achieve with a single mesh, even in relatively simple two-dimensional geometries, usually because the grid cannot be effectively adapted to geometric features having high curvature. This is especially disadvantageous in turbomachine application where it is essential to resolve accurately the viscous and turbulent flow around the leading and trailing edges. The advantage derived in this environment from the multiblock strategy, in which the H/O-grid in Figure 11 is adopted, is indicated in Figure 12 by a comparison of pressure contours close to the leading edge. As can be seen, the 'kink' in the pressure contours returned by the H-type grid (Figure 12(a)) is not present in the solution obtained with the H/O-mesh (Figure 12(b)). Computational results have been obtained with Launder and Sharma's low-Re k–ϵ model[14] for an inlet flow angle of 46°, representing extreme off-design conditions in which the blade is highly loaded and for which losses are high. Solutions for the profiles of streamwise velocity at three locations on the blade suction side are shown in Figure 13. It is noted that there is close agreement between the results returned by the two grids, although the H/O-grid resolves considerably better the flow structure close to the leading and trailing edges, the former having been demonstrated in Figure 12.

With the validity of the multiblock scheme established, the predictive performance of three turbulence closures are examined next. The models are the linear eddy-viscosity variants of Launder and Sharma[14] and Lien and Leschziner[15] and the non-linear variant of Craft *et al.*[16] The designation 'non-linear' signifies that the Reynolds stresses are related to higher-order expansions of strain and vorticity tensors, with the eddy viscosity being a coefficient of proportionality in each and every

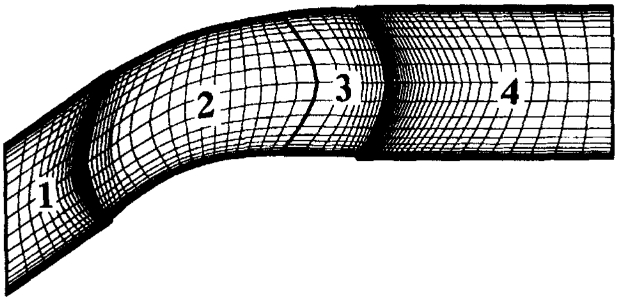

Figure 9. H-grid (either single-block or multiblock) in CD compressor-cascade passage

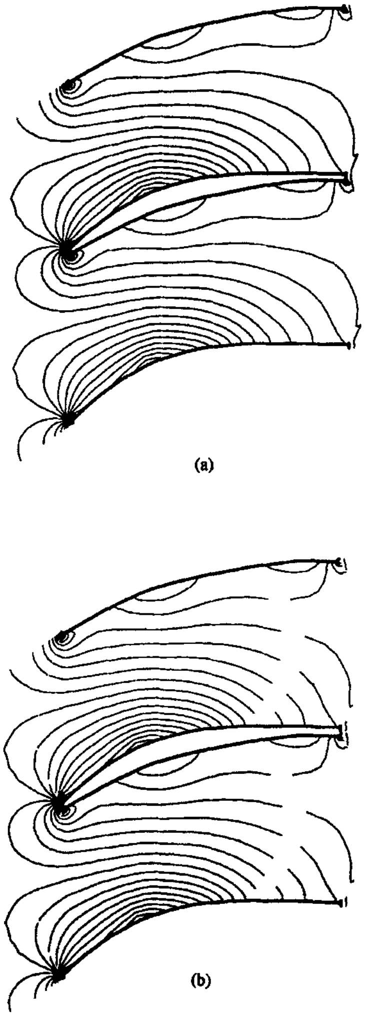

Figure 10. Pressure contours in compressor-cascade passage, (a) with single-block solution and (b) with multiblock solution

additive term of the expansion. This approach aims to return, at least in some measure, the anisotropy of turbulence and its interaction with curvature and normal straining. Calculations have been performed for various incidence angles ranging from 25° to 46°.[17] Here, only the 46° case is presented, in which the suction-side flow is close to the 'stall' condition.

Variations of the boundary-layer, displacement and momentum thicknesses on both pressure and suction sides are given in Figure 14. A key process to resolve is the response of the turbulence model during the initial development phase of the boundary layer over the suction side. Evidently, there exists a laminar separation bubble close to the leading edge, with the flow being transitional and becoming turbulent in the vicinity of the reattachment point. The linear model fails entirely to resolve this feature, while the non-linear model responds much more sensitively, predicting a much more rapid thickening of the boundary layer at the leading edge and hence higher losses in the fully turbulent region.

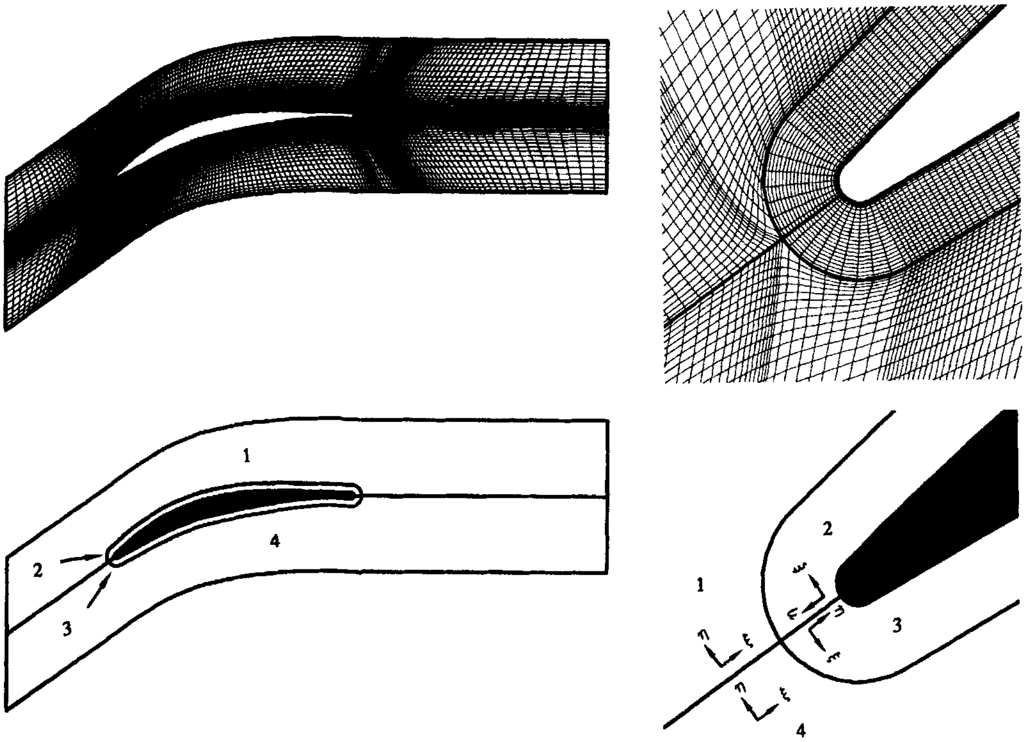

Figure 11. H/O-multiblock arrangement around compressor-cascade blade, with zoom on leading edge and associated local co-ordinate systems

Consistent with the above is the behaviour of the pressure distribution along the suction side, shown in Figure 15. The tendency towards separation at the leading edge, resolved by the non-linear model, is accompanied by a more gentle increase in pressure in this region. Moreover, the pressure plateau on the suction-side base is captured, suggesting a tendency towards stall as the trailing edge is approached.

3.3. NLR 7301 multielement aerofoil

This second application example is a two-element aerofoil, designed on the basis of an early supercritical section having the same designation. The main feature of this configuration is that it provides very high lift at high incidence without flow separation being provoked along the suction sides, apart from a small laminar separation bubble on the leading edge. Because the near-surface flow is in the form of an attached boundary layer, albeit thick and decelerating, the interaction between turbulence and curvature has less impact on the mean-flow features than it did in the previous case, and calculations have therefore only been performed with the linear eddy-viscosity model. The operational conditions are detailed in Section 3.1, and these have been chosen because the associated flow is close to the state of maximum lift and for the availability of especially detailed measurements.

No-slip and impermeability conditions were prescribed at the aerofoil surface. At the far-field boundary, 10 chords away from the centre of the aerofoil, the freestream velocity was specified. The transition on the suction and pressure sides of the main wing was induced artificially at $x/c = 0{\cdot}03$

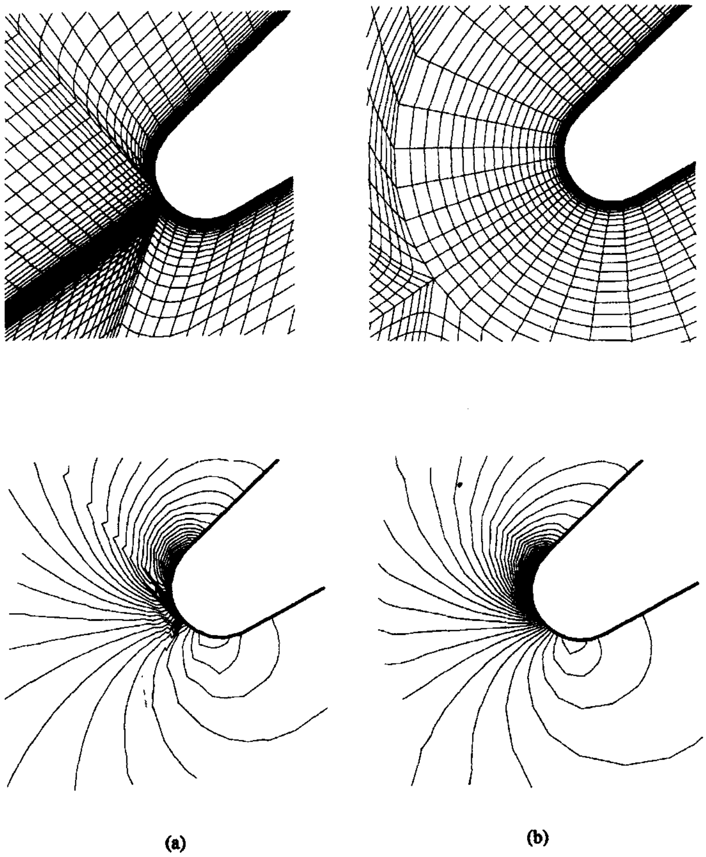

(a) (b)

Figure 12. Pressure contours around leading edge of compressor-cascade blade, (a) with single-block H-grid and (b) with multiblock H/O-grid

and 0·7, respectively, in accord with the measurements. On the flap, transition was induced at $x/c = 1{\cdot}08$ on the suction side, while the flow on the pressure side was assumed laminar.

The computational grid and the block topology, supplied by Saab, are shown in Figure 16. The flow domain is subdivided into nine blocks, containing 36,208 cells. Particular attention is drawn to block 1 which abbuts blocks 7 and 8 at the eastern face, a condition requiring the introduction of special steps in the connectivity matrices MATRIX and COORD described in Section 2. The modified forms are as follows:

MATRIX(BLOCK, FACE, N-of-NEIGHBOURS)
COORD(BLOCK, FACE, N-of-NEIGHBOURS)

and N-of-NEIGHBOURS denotes the maximum number of neighbours in relation to each face. In the case of BLOCK = 1 where N-of-NEIGHBOURS = 2,

MATRIX(1,1,1) = 7, MATRIX(1,1,2) = 8,
MATRIX(1,2,1) = 9, MATRIX(1,2,2) = − 1,
MATRIX(1,3,1) = 0, MATRIX(1,3,2) = − 1,
MATRIX(1,4,1) = 0, MATRIX(1,4,2) = − 1,

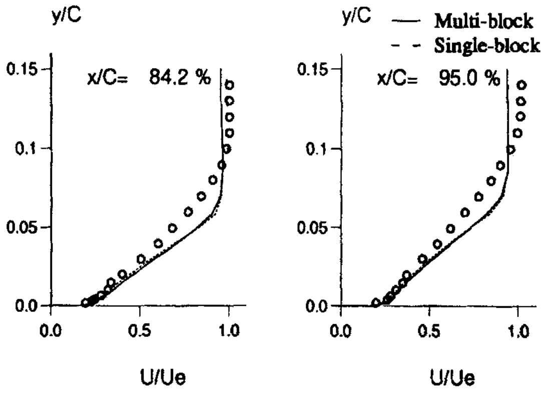

Figure 13. Velocity profiles in boundary layer on suction side of compressor-cascade blade, predicted with H- and H/O-grid

and

COORD(1,1,1) = 1, COORD(1,1,2) = 5,
COORD(1,2,1) = 5, COORD(1,2,2) = − 1,
COORD(1,3,1) = 0, COORD(1,3,2) = − 1,
COORD(1,4,1) = 0, COORD(1,4,2) = − 1.

The value ' − 1' above signifies that the associated element in the MATRIX or COORD array is redundant owing to the fact that the number of neighbours along that face is less than N-of-NEIGHBOURS. An alternative approach to adopting the block topology shown in Figure 16 involves a further subdivision so as to ensure that each block face interfaces only one neighbour, allowing the original connectivity practices to be retained.

Computational results for wall pressure and skin friction are compared with experimental data in Figures 17 and 18 respectively. As can be seen, there is close agreement in respect of pressure distributions around both the main aerofoil and the flap, confirming the view that in attached flow

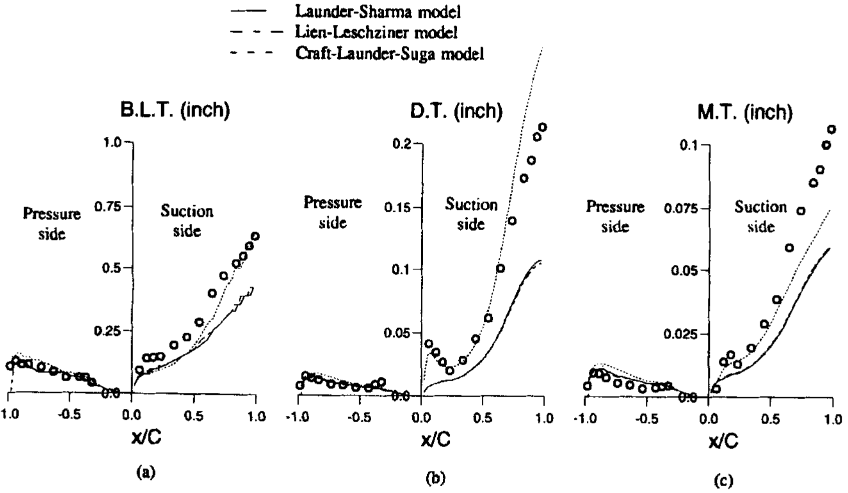

(a) (b) (c)

Figure 14. Boundary-layer parameters associated with different turbulence models around compressor-cascade blade: (a) boundary-layer thickness; (b) displacement thickness; (c) momentum thickness

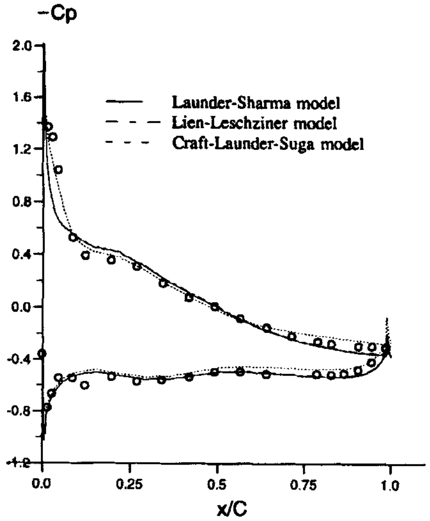

Figure 15. Surface pressure predicted with different turbulence models around compressor-cascade blade

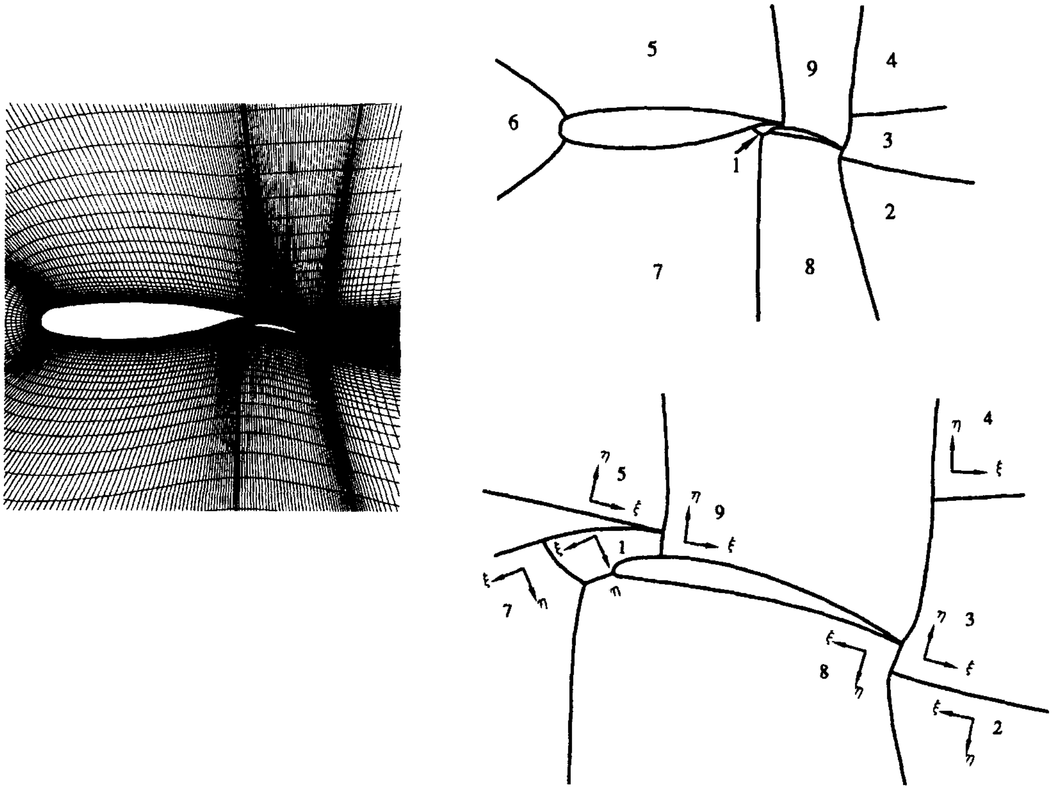

Figure 16. Multiblock arrangement and mesh used for NLR two-element high-lift aerofoil

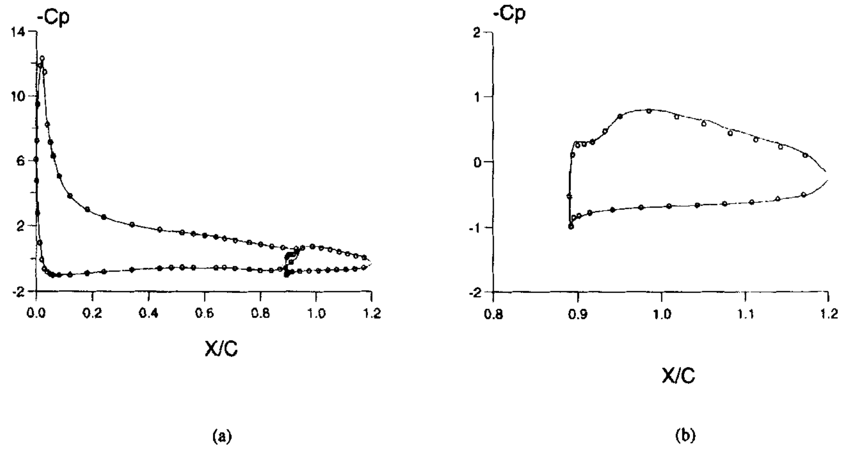

Figure 17. Surface-pressure distributions (a) around NLR two-element configuration and (b) around flap

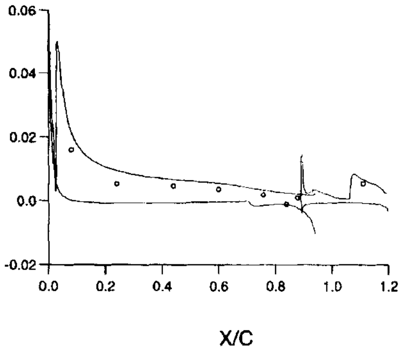

Figure 18. Skin friction around NLR two-element configuration

conditions the principal operational parameters—the lift and pressure drag—are rather insensitive to turbulence modelling. Comparisons with the rather limited skin-friction data in Figure 18 are not very informative, but seem to suggest that skin friction is overestimated at large incidence when the adverse pressure gradient is high. This is in accord with the general view that the linear eddy-viscosity k–ϵ model generates excessive levels of turbulence energy as well as turbulent length-scale values in curved boundary layers subjected to adverse pressure gradient, owing to a combination of insufficient sensitivity to convex curvature and defects in the ϵ-equation. Detailed comparisons with experiments for boundary-layer profiles and Reynolds stresses can be found in Reference 18.

3.4. Circular-to-rectangular transition duct

A perspective 3D view of the CR duct and plots of two cross-sectional grids at the duct-exit plane, associated with different block topologies, are given in Figure 19. The total numbers of grid nodes in the block arrangements of Figure 19(a) and 19(b) are 180,000 and 163,300 respectively. The

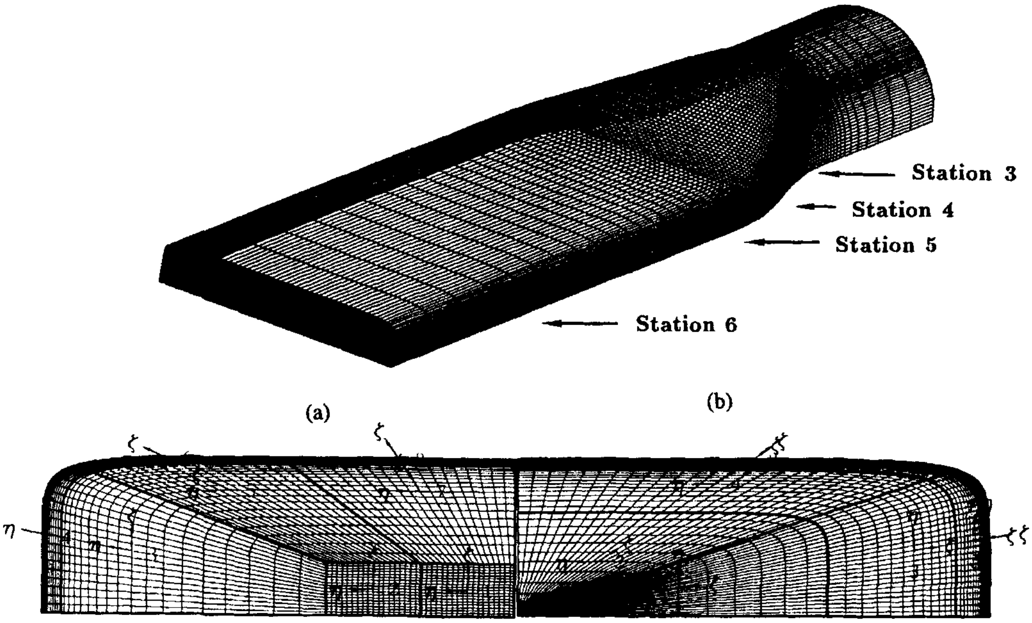

Figure 19. Mesh and multiblock arrangement for 3D transition duct

operation of the multiblock scheme is here demonstrated by way of a computation with the low-*Re* k–ϵ model of Lien and Leschziner.[15] A companion study of the same configuration by Lien and Leschziner[19] presents computations with several turbulence models, including second-moment closure.

Circumferential distributions of the wall-pressure coefficient C_p, computed at four different axial stations, are compared with experimental data in Figure 20. It is instructive to consider these distributions in conjunction with the secondary-velocity fields given in Figure 21, since there is a direct causal relationship between transverse motion and pressure gradient. As can be seen, the level of C_p increases up to station 3, implying deceleration, and decreases towards station 5, signifying acceleration. Thereafter the flow tends to recover towards an established constant-area duct flow, and the pressure tends to become uniform at station 6. Owing to vertical constriction and horizontal elongation in the cross-sectional shape, the pressure at $S/S_{\max} = 0$ (centre of the upper wall) develops a maximum, while the pressure at $S/S_{\max} = 1$ (centre of the side wall) reaches a minimum. This induces a sideways motion along the upper wall towards the side walls, which is the first stage leading to the formation of the transverse vortices. Beyond station 3 the curvature on both upper and side walls reverses its sign and this counteracts (but does not reverse) the above process.

Finally, circumferential skin-friction distributions are shown in Figure 22. Two prominent features are the depression in C_f at about $S/S_{\max} = 0{\cdot}75$ and the decline in C_f as the centre of the side wall, $S/S_{\max} = 1$, is approached. The former is due to the suppression of momentum in the boundary layer arising from the combined influence of the upper and side walls at the (rounded) corner of the rectangular duct. The latter reflects the transport of low-momentum fluid towards the side wall by the

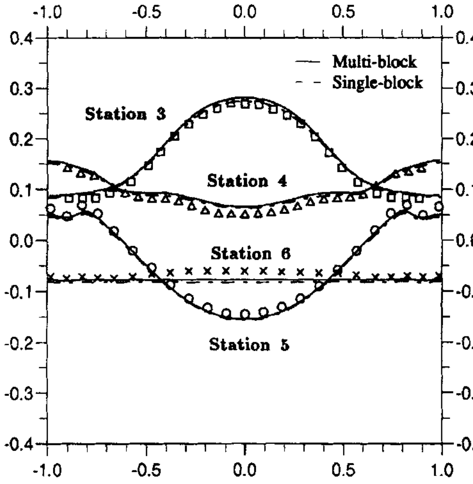

Figure 20. Circumferential wall-pressure variations at different axial locations of transition duct, predicted with two grids of Figure 19

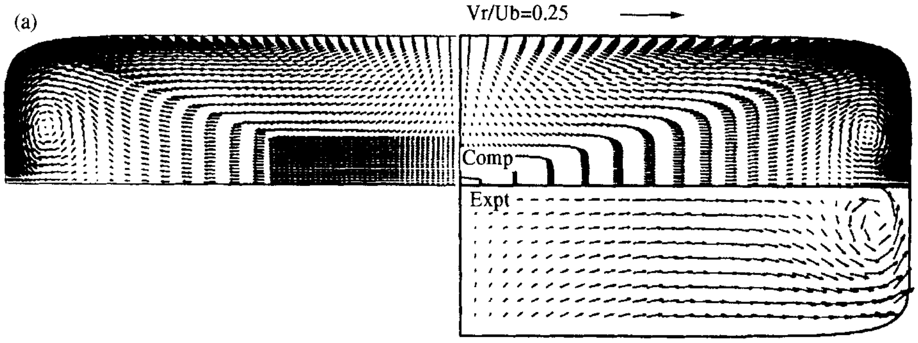

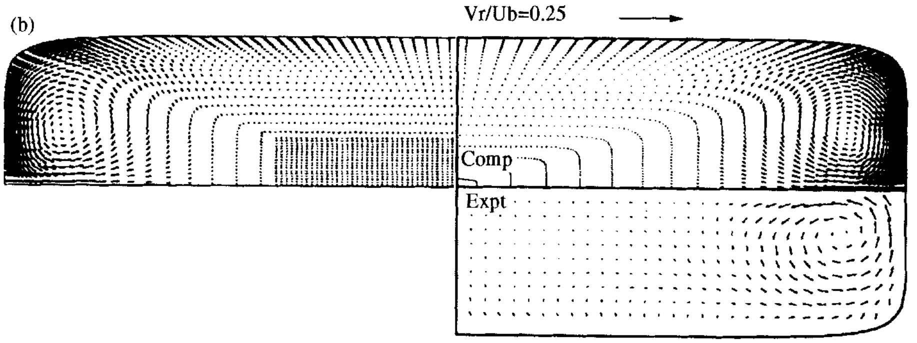

Figure 21. Transverse motion in sections 5(a) and 6(b) of transition duct, predicted with two grids of Figure 19, compared with experimental data

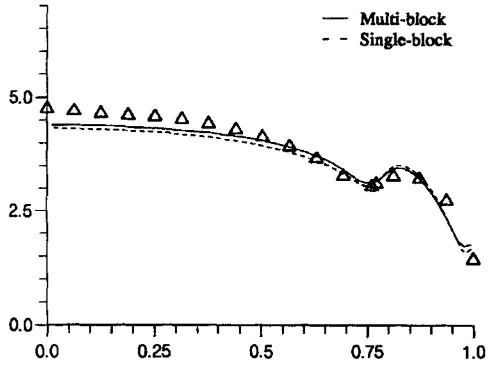

Section 5

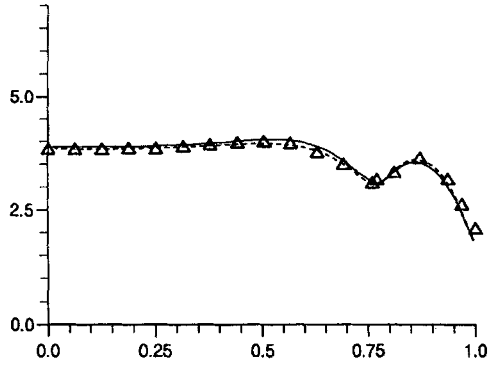

Section 6

Figure 22. Streamwise skin-friction coefficient at stations 5 and 6 of transition duct, predicted with two grids of Figure 19

transverse circulation. Overall, the predictions agree fairly well with the experiment, with virtually no dependence on the grid topology being observed.

4. CONCLUSIONS

The formulation and implementation of a general multiblock algorithm for complex turbulent flows have been addressed in detail. The algorithm couples, in an unstructured manner, finite volume blocks in which the grid is structured but non-orthogonal and in which the equations are solved on a fully collocated grid by a pressure-correction algorithm.

The main impetus for the extension is the need to secure geometric flexibility in flows in which turbulence transport is of crucial importance and in which numerical accuracy is essential, especially close to surface features of high curvature.

Since the present algorithm allows the computational domain to be decomposed into arbitrary sets of blocks, with block-topology information stored in dedicated connectivity matrices, the execution on parallel computers is a natural and straightforward option.

Although grid generation within a block-structured approach, especially for very complex 3D geometry, can be tedious and time-consuming, the retention of a structured topology offers undisputed advantages when complex turbulence models are used to resolve near-wall processes.

Moreover, the retention of a simple local indexing system eases vectorization. However, because of the adoption of a 'block Jacobi', method, in conjunction with a segregated solution sequence, the convergence rate tends to deteriorate as the number of blocks increases. The level and rate of deterioration depend on numerous factors, however, among them the range of nodes-to-block ratio, the detailed block topology across the solution domain, the linear solver used within blocks and the complexity of the flow physics and turbulence model. A test in which the number of blocks used for the case of the CD compressor cascade, considered in Section 3.2, was increased from four to eight yielded an increase in CPU time of only 2 per cent. However, this figure is likely to rise non-linearly as the number of blocks increases. This deficiency can be addressed by using geometric or algebraic multigrid methods—an issue to be considered in a future paper.

ACKNOWLEDGEMENTS

Parts of this study were supported by a grant from Rolls Royce p.l.c. in Derby, and Defence Research Agency (DRA), UK, for which the authors are grateful. Some of the computations were performed on the Cray YMP computer at the Rutherford Appleton Laboratory and the Fujitsu VPX 240 machine at the Manchester Computer Centre, in both cases with allocations granted by the U.K. Science and Engineering Research Council.

APPENDIX: FORTRAN code fragment showing the use of Cray YMP parallel compiler directives in the solution of a Laplace equation

```
                        SUBROUTINE LAPLACE
                        ⋮
                        COMMON BLOCKS
                        ⋮
              C
                        NSWPU=4
              C
              CFPP$     SELECT CONCUR
P------                 DO 1000 NB=1, NO-of- BLOCKS
P             C
P N-----                DO 10 K=NKBEG(NB)+2, NKEND(NB) - 2
P N N---                DO 10 J=NJBEG(NB)+2, NJEND(NB) - 2
P N N V-                DO 10 I=NIBEG(NB)+2, NIEND(NB) - 2
P N N V                 AP(I,J,K)=6.
P N N V                 AE(I,J,K)=1.
P N N V                 AW(I,J,K)=1.
P N N V                 AN(I,J,K)=1.
P N N V                 AS(I,J,K)=1.
P N N V                 AT(I,J,K)=1.
P N N V                 AB(I,J,K)=1.
P N N V                 SP(I,J,K)=0.
P N N V                 SU(I,J,K)=0.
P N-N-V-                10CONTINUE
P             C
```

```
P------            1000CONTINUE
             C
N------            DO NS = 1, NO-of-SWEEPS
N            CFPP$ CNCALL
N P-----           DO NB = 1, NO-of-BLOCKS
N P                CALL MATRIX-SOLVER(NB,PHI)
N P-----           END DO
N            CFPP$ CNCALL
N P-----           DO NB = 1, NO-of-BLOCKS
N P                CALL MESSAGE-PASS(NB,PHI)
N P-----           END DO
N            C
N------            END DO
                   RETURN
                   END
```

N: Loop not optimized or not selected.
V: Vector construct; FPP vectorizes.
P: Parallel construct; FPP autotasks.

REFERENCES

1. S. C. Caruso, J. H. Ferziger and J. Oliger, 'Adaptive grid techniques for elliptic fluid-flow problems', *Rep. TF-23*, Department of Mechanical Engineering, Stanford University, 1985.
2. R. L. Davis and J. F. Dannenhoffer, 'Decomposition and parallization strategies for adaptive grid-embedding techniques', *Comput. Fluid Dyn.*, **1**, 79 (1993).
3. W. L. Chen, F. S. Lien and M. A. Leschziner, 'A local grid refinement scheme within a multiblock structured-grid strategy for general flows', *Proc. 6th Int. Symp. on Computational Fluid Dynamics*, Lake Tahoe, NV, September 1995.
4. F. S. Lien and M. A. Leschziner, 'A general non-orthogonal finite-volume algorithm for turbulent flow at all speeds incorporating second-moment closure, Part 1: Numerical implementation, Part 2: Application', *Comput. Methods Appl. Mech. Eng.*, **114**, 123, 149 (1994).
5. B. P. Leonard, 'A stable and accurate convective modelling procedure based on quadratic upstream interpolation', *Comput. Methods Appl. Mech. Eng.*, **19**, 59 (1979).
6. F. S. Lien and M. A. Leschziner, 'Upstream monotonic interpolation for scalar transport with application to complex turbulent flows', *Int. J. Numer. Methods Fluids*, **19**, 527 (1994).
7. S. V. Patankar, *Numerical Heat Transfer and Fluid Flow*, McGraw-Hill, New York, 1980.
8. C. M. Rhie and W. L. Chow, 'Numerical study of the turbulent flow past an aerofoil with trailing edge separation', *AIAA J.*, **21**, 1525 (1983).
9. F. S. Lien and M. A. Leschziner, 'Multigrid acceleration for turbulent flow with a non-orthogonal, collocated scheme', *Comput. Methods Appl. Mech. Eng.*, **118**, 351 (1994).
10. Y. Elazar and R. P. Shreeve, 'Viscous flow in controlled diffusion compressor cascade with increasing incidence', *ASME Paper 89-GT- 131*, 1989.
11. B. van den Berg, 'Boundary layer measurements on a two-dimensional wing with flap', *NLR TR 79009U*, 1979.
12. J. H. M. Gooden and M. van Lent, 'Hot-wire measurements in the two- dimensional wing wake above a trailing edge flap at a condition close to maximum lift', *NLR CR 91038C*, 1991.
13. D. O. Davis and F. Gessner, 'Experimental investigation of turbulent flow through a circular-to-rectangular transition duct', *AIAA Paper 90-1505*, 1990.
14. B. E. Launder and B. I. Sharma, 'Application of energy-dissipation model of turbulence to the calculation of flow near a spinning disc', *Lett. Heat Mass Transfer*, **1**, 131 (1974).
15. F. S. Lien and M. A. Leschziner, 'Computational modelling of 3D turbulent flow in S-diffuser and transition ducts', in *Engineering Turbulence Modelling and Measurements 2*, Elsevier, Amsterdam, 1993, p. 217.
16. T. J. Craft, B. E. Launder and K. Suga, 'Extending the applicability of eddy viscosity models through the use of deformation invariants and non-linear elements', *Proc. 5th Int. Symp. on Refined Flow Modelling and Turbulence Measurements*, Paris, 1993, p. 125.

17. W. L. Chen, F. S. Lien and M. A. Leschziner, 'Computational modelling of cascade-blade flow with linear and non-linear low-*Re* eddy-viscosity models', *AGARD-CP-571 Loss Mechanism and Unsteady Flows in Turbomachinery*, p. 3.1, 1995.
18. F. S. Lien, W. L. Chen and M. A. Leschziner, 'Computational modelling of a high-lift aerofoils with turbulence-transport models', *Proc. CEAS Eur. Forum on High Lift and Separation Control*, p. 10.1 Bath, 1995.
19. F. S. Lien and M. A. Leschziner, 'Second-moment closure for three-dimensional turbulent flow around and within complex geometries', *Comput. Fluids*, **25**, 237 (1996).